Real-Time H_∞ Control of Networked Inverted Pendulum Visual Servo Systems

Dajun Du, Changda Zhang, Yuehua Song, Huiyu Zhou, Xue Li, Minrui Fei, Wangpei Li

Abstract—**Aiming at the challenges of networked visual servo control systems, which rarely consider network communication duration and image processing computational cost simultaneously, we here propose a novel platform for networked inverted pendulum visual servo control using H_∞ analysis. Unlike most of the existing methods that usually ignore computational costs involved in measuring, actuating and controlling, we design a novel event-triggered sampling mechanism that applies a new closed-loop strategy to dealing with networked inverted pendulum visual servo systems of multiple time-varying delays and computational errors. Using Lyapunov stability theory, we prove that the proposed system can achieve stability whilst compromising image-induced computational and network-induced delays and system performance. In the meantime, we use H_∞ disturbance attenuation level γ for evaluating the computational errors, whereas the corresponding H_∞ controller is implemented. Finally, simulation analysis and experimental results demonstrate the proposed system performance in reducing computational errors whilst maintaining system efficiency and robustness.**

Index Terms—**Inverted pendulum, visual servo, computational delay, computational error, network-induced delay, real-time H_∞ control.**

I. INTRODUCTION

AS ONE of the representative developments in the control field, effective manipulation and control of inverted pendulum systems (IPSs) have demonstrated promising progress in handling some challenging problems such as nonlinearity, robustness, stability and tracking [1]–[4]. In the last 10-20 years, the traditional IPSs have been transformed to networked IPSs where inverted pendulums, sensors and controllers distributed at different locations can exchange and share information via networks [5]. Recently, with the advances of visual sensing technology, many industrial applications, e.g. automated detection and robot control, have started integrating visual observations such as images with a networked IPS in order to create a fully functioning cyber-physical system (CPS) [6]–[11]. Among the applications, networked inverted pendulum visual servo systems (NIPVSSs) have gained large

attention in the community, which work with the interplay of control, computation and communication (3C).

Smart devices, e.g. the IPSs which involve visual measurements, deploy machine vision technologies for processing visual inputs in order to achieve visual servo feedback control. This control process very likely introduces image-induced computational delay (i.e., delay induced by the image processing time) and computational errors (i.e., computational errors of image processing), which affect the performance of the control system and cause instability of the system. This practical challenge strongly motivates people to develop an effective and efficient system of the NIPVSSs for better system performance.

However, most of the existing systems only consider the communication and control issues, whilst ignoring the computational issues. In this paper, we present a novel NIPVSS, jointly considering communication networks and visual servo, where the former causes network-induced delay and the latter causes image-induced computational delay and errors. To handle the 3C issues in a challenge environment, this paper aims to address the control problem of the NIPVSSs in the presence of network-induced and image-induced computational delay and computational errors. The main contributions of this paper are summarised as follows:

1) A closed-loop system strategy to handle multiple time-varying delays and computational errors is established. The time-varying delay include image-induced computational delay and network-induced delay, which are modeled and treated in different channels. The disturbance and interference due to image processing errors, which have not been investigated in the previous works, are investigated here with comprehensive statistical analysis.

2) An H_∞ stability condition is derived to guarantee stability whilst compromising image-induced computational and network-induced delays and system performance. In the meantime, H_∞ disturbance attenuation level γ is employed to evaluate the computational errors, and the stabilizing controller design is rendered.

3) A new intelligent platform for implementing the NIPVSS is constructed. The new feature of this system is that communication networking and visual servo are jointly considered in the process, where network-induced delay may be due to network quality, traffic congestion or limited bandwidth. In order to obtain cart positions and pendulum angles from the images, captured by the visual sensors, our proposed system must deal with time-varied variables of communication networks and image processing models.

The remainder of this paper is organized as follows. In Section II, we review the existing studies for real-time control of the IPSs with the focus on previous attempts on networked or computational constraints in a general style. In Section III, the framework of the NIPVSS is firstly constructed, and then the problems related to the 3C concerns are analyzed for establishing a closed-loop NIPVSS to handle different time-varying delay and computational errors. The stability analysis and controller design are presented in Section IV. Afterwards, Section V reports the experimental set-up and results, and discusses the experimental results for the NIPVSS. Conclusions and future work are given in Section VI.

II. RELATED WORK

In this section, we substantially review the previous works on the IPSs related to networked and computational constraints. The unique features of our work are then discussed as well.

A. Real-Time Control of the IPSs with Networked Constraints

A number of studies on the networked IPSs have been reported [12]–[14]. The networked IPS is modeled as a control system with state and input delays, and sliding mode control is commonly used to achieve stable control [12]. The networked IPS is established as a time-delay system model, and different stability conditions are analyzed via Lyapunov functions [13]. In [14], the event-triggered control problem for linear time-delay systems is investigated, where the control parameters are optimized by adjusting the weights of the quadratic cost function and the event-triggered parameters to improve the proposed method in the networked IPS. However, the effectiveness of the proposed methods described in the above studies is only justified in simulations, and there are very few studies that use real experiment to validate the proposed approaches.

In this paper, a novel NIPVSS is proposed to address the network-induced delay problem. The statistical characteristics of network-induced delay is analyzed and its impact on the control system is then explored.

B. Real-Time Control of the IPSs with Computational Constraints

Visual servo firstly proposed by Hill and Park [15] is a closed-loop control strategy based on visual information feedback and has been widely applied in many areas such as agriculture automation [16], industrial automation [17], [18], intelligent medical instruments [19], and automated vehicle navigation [20]. The problems such as visual sensing delay may be caused by the uncertainty of visual measurement and the changes in the environments such as background and illumination [21], [22], which may deteriorate the performance of visual servo systems and even cause system instability. By introducing visual servo into the IPS, we generate the visual servo-based IPS with certain computational time for image acquisition and processing. According to image-induced computational delay, the existing research studies can be divided into two categories:

(1) Ignoring image-induced computational delay [22]–[24]: In [22] and [23], only pendulum angles are obtained using visual sensors. In [24], all state information of the cart and the pendulum is detected by the visual sensors. However, none of the above studies considers the effect of image-induced computational delay on the stability performance. To achieve high quality control, it is necessary to reasonably restrict the image processing time so as to achieve real-time control of the visual servo-based IPS.

(2) Considering image-induced computational delay [25], [26]: All state information of the IPS is detected by visual sensors but image-induced computational delay is a constant [25]. In [26], the detection method is the same as that of [25], and the effect of image processing time on the IPS is analyzed. However, the above studies do not analyze specific characteristics of the image processing elements.

In this paper, unlike the existing IPS that ignore image-induced computational delay or regard it as a constant delay whilst ignoring image processing errors, we propose real-time computational methods for vision sensing measurements to obtain cart positions and pendulum angles. A new event-triggered sampling mechanism of visual sensors is designed according to the statistical characteristics of the image processing elements and computational errors.

C. Real-Time Control of the NIPVSSs with Networked and Computational Constraints

An NIPVSS needs to handle the 3C challenges that have been reported in [27], which reveal the relationship between the networked constraints (e.g., network-induced delay, data packet dropout, etc. [28]–[30]) and the system stability whilst ignoring the effect of the computational time on the controller design. In the meantime, due to the large number of image data, the impact of the computational load on the system performance cannot be ignored. For example, the data of networked visual servo robots will affect the performance of the control system because of the data amount and the network-induced delay.

For networked visual servo robots, network-induced delay and image-induced computational delay are contributing to the total delay in the stability analysis [31]–[34]. In fact, these two delay mechanisms hold different properties. The former is due to limited network communication bandwidth and unbalanced network load, whilst the latter is caused by image processing tasks.

In this paper, network-induced delay and image-induced computational delay are not part of the total delay changing over time. Meanwhile, different from networked visual servo robots, the effect of image processing errors is considered, and network-induced and image-induced computational delays in the NIPVSSs are characterized. The relationship between these factors and the performance of the NIPVSSs is quantified.

III. PROBLEM FORMULATION

A. The Framework of the NIPVSS

In this paper, we propose an NIPVSS to deal with the inverted pendulum under networked and computational constraints.
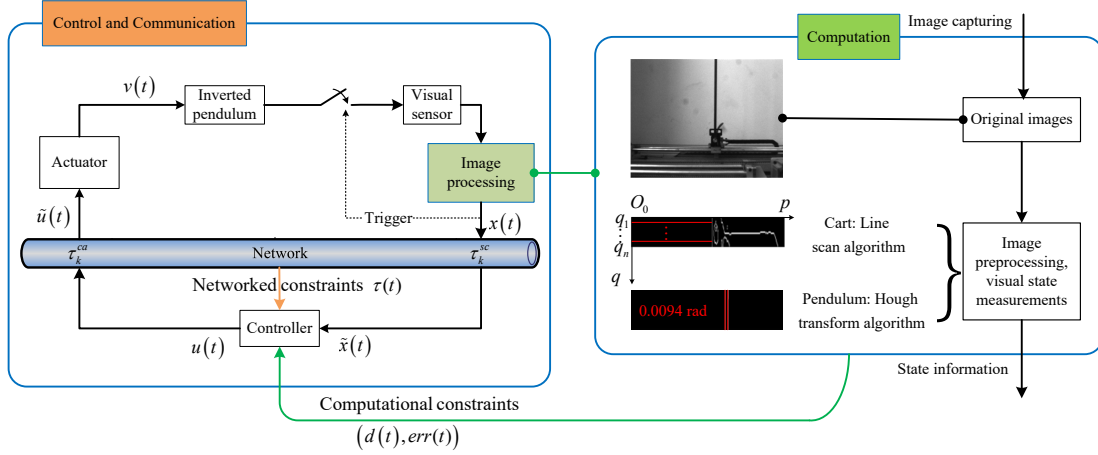
Fig. 1. Framework of the NIPVSS.

Fig. 1 outlines the framework of the NIPVSS.

Remark 1: The NIPVSS is a typical CPS, which integrates image processing computation, communication and control algorithms. Compared against the IPS involving communication network and relying on the simulation approach, the NIPVSS in this paper is achieved on an experimental platform, and the control algorithm for that purpose is designed according to both networked and computational issues. Our work is dedicated to providing theoretical basis and technical support to achieve real-time industrial visual servo control.

As can be seen from Fig. 1, the real-time moving images of the IPS captured by the industrial camera based on an event-triggered strategy (See Section I of the supplementary materials for image capturing) is sent to the image processing component to extract the state information of the pendulum angles and the cart positions, and the acquired state information is sent to the remote controller via networks. Afterwards, the corresponding control signals are processed by the control component to achieve stable control of the IPS. However, there are three problems engaging the 3C in the proposed NIPVSS as shown in Fig. 1.

Remark 2: Unlike the threshold-based event-triggered sampling condition, based on the latest transmitted sample-data [35]–[41], the event-triggered sampling condition proposed in this paper depends on the image processing unit. After the image processing of the current image frame has been completed and the inverted pendulum has changed its state, the camera will be triggered to capture the next frame.

Computation: Using the visual sensors, the motion images that include the state information of the IPS can be continuously captured. However, the physical variables such as cart positions and pendulum angles are unable to be directly acquired so image processing is requested to provide the state information from the captured images. The whole procedure of image processing (See Section I of the supplementary materials for the detailed description) is outlined on the right-hand side of Fig. 1, which mainly includes the original images, image preprocessing (e.g. line interception and Canny edge detection) and visual state measurements.

Furthermore, the changes of the environmental background

and illumination affect the image quality and the image processing time that is statistically estimated and shown in Section II.A of the supplementary materials. We denote the image processing time and the lower and upper bounds of the delay by

$$
\begin{cases}
d_k \in [\underline{d}, \bar{d}] \\
\underline{d} = 0.019s \\
\bar{d} = 0.029s.
\end{cases} \tag{1}
$$

The computational errors of the state variables are denoted as:

$$
err(t) = B_w w(t) \tag{2}
$$

where $B_w = \begin{bmatrix} 0.0016 & 0.0071 & 0.0751 & 0.3510 \end{bmatrix}^T$, $w(t) \in (-1, +1)$ guaranteeing $w(t) \in \mathcal{L}_2(0, \infty)$.

Remark 3: According to the statistical analysis of computational errors $err(t)$ (See Section II.B of the supplementary materials), the cart position, cart velocity, pendulum angle, and pendulum angular velocity in $err(t)$ are time-varied with the ranges of $[-0.0015, +0.0015]$, $[-0.007, +0.007]$, $[-0.075, +0.075]$ and $[-0.35, +0.35]$. When each element in B_w is set to be slightly bigger than the corresponding upper bound of the above statistical results, namely $B_w = \begin{bmatrix} 0.0016 & 0.0071 & 0.0751 & 0.3510 \end{bmatrix}^T$, and it follows that $w(t) \in (-1, +1)$ and $\|w(t)\| < 1$, which leads to

$$
\|w(t)\|_2 \triangleq \left(\int_0^\infty \|w(t)\|^2 dt \right)^{1/2} < \infty.
$$

This guarantees that $w(t) \in \mathcal{L}_2(0, \infty)$.

Statistical analysis shows that the image processing time and errors are time-varied and bounded which significantly affect the stability of the IPS.

Remark 4: Different from the fixed condition shown in [22], the image processing time in (1) is time-varied and bounded. This severely affects the performance and stability of the IPS (e.g. when the image processing time is larger than 34ms, the IPS fails to work). Moreover, as can be seen from (2), the computational error is time-varied and bounded. After the computational error has been calculated, a larger control input error will be brought in (e.g. if the pixel displacement error

of the cart is 2 pixels, the corresponding control input error will become $5.83 m/s^2$), causing an instable IPS. Therefore, the influence of the image processing time and errors on the system performance cannot be ignored in this study.

Communication: As shown in the left-hand side of Fig. 1, when information are transmitted through the network, network-induced delay occurs in the transmission over the network due to limited communication bandwidth and unbalanced network load [42]–[44]. We denote network-induced delay from the visual sensor to the controller and the network-induced delay from the controller to the actuator by τ_k^{sc} and τ_k^{ca}, respectively.

Control: As mentioned above, the NIPVSS's performance is affected by image-induced computational delay (i.e., delay induced by the image processing time) and errors and network-induced delay. To achieve stable control of the NIPVSS, the relationship between the control performance and 3C parameters (i.e. image-induced computational delay, computational errors and network-induced delay) need to be established. Furthermore, based on such relationship, the controller can be designed using a method such as Lyapunov stability approach.

Considering time-varying image-induced computational delay, computational errors and network-induced delay and the requirements of efficiently and accurately controlling the NIPVSS, it is important to establish a closed-loop model, analyze the system stability and design the controller.

B. The Closed-Loop Model of the NIPVSS

TABLE I
DETAILED MODEL PARAMETERS

Parameter	Physical meaning	Value
l	Length from the pivot to the center of the pendulum	0.25m
m	Mass of the pendulum	0.109kg
J	Moment of inertia of the pendulum	0.009083kg·m^2
g	Acceleration of gravity	9.81m/s^2
α	Cart position	m
θ	Pendulum angle	rad

According to Lagrange's equations and linearization within the range ($|\theta| \leqslant 0.2$ rad), the state-space equation of the inverted pendulum is modelled as follows, whilst the parameters of the inverted pendulum are given in Table I.

$$\begin{cases} \dot{x}(t) = Ax(t) + Bv(t) \\ z(t) = Cx(t) + Dv(t) \end{cases} \quad (3)$$

where $x(t) \in \Re^4$ is the state vector and $x_1 = \alpha, x_3 = \dot{\alpha}, x_2 = \theta, x_4 = \dot{\theta}$ defines the cart position, cart velocity, pendulum angle and angular velocity, respectively. $v(t) \in \Re$ is the actuator's output signal, i.e., the cart acceleration. $z(t) \in \Re^2$ is the controlled output. A, B, C, D are constant matrices with appropriate dimensions which are given bellow.

$$A = \begin{bmatrix} 0 & 0 & 1 & 0 \\ 0 & 0 & 0 & 1 \\ 0 & 0 & 0 & 0 \\ 0 & \frac{lmg}{J} & 0 & 0 \end{bmatrix}, B = \begin{bmatrix} 0 \\ 0 \\ 1 \\ \frac{ml}{J} \end{bmatrix}$$
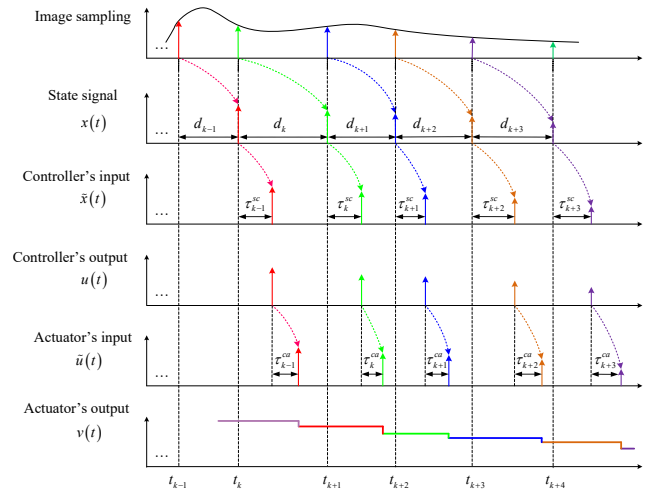

Fig. 2. Signal's timing diagram of the NIPVSS.

$$C = \begin{bmatrix} 1 & 0 & 0 & 0 \\ 0 & 1 & 0 & 0 \end{bmatrix}, D = \begin{bmatrix} 0 \\ 0 \end{bmatrix}.$$

Remark 5: Generally, there are two approaches of modelling system (3) according to different control input variables. One is to define the external force on the cart as the control input variable [45], and another is to define the cart acceleration $v(t)$ as the control input variable [46]. The second method is employed in this paper.

Next, a full state feedback controller is designed, i.e.,

$$u(t) = Kx(t) \quad (4)$$

where K is the feedback gain.

For obtaining the controller $u(t)$ in (4), the signal's timing diagram of the NIPVSS is shown in Fig. 2, which is divided into six steps as follows:

1) The real-time moving images of the IPS are captured by using the above proposed event-triggered strategy, i.e., the images are sampled at the instants $\{t_{k-1}, t_k, t_{k+1}, \ldots\}$.

2) For each captured image (e.g., the captured image at the sampling instant t_k), the state signal $x(t)$ is acquired after some time has been spent on the image processing (i.e., d_k),

$$x(t) = x(t_k), t \in \{t_k + d_k, k = 0, 1, 2, \ldots\}.$$

3) The above state signal $x(t)$ is transferred to the controller with network-induced delay τ_k^{sc}, so the controller receives $x(t)$ at the instant $t_k + d_k + \tau_k^{sc}$, i.e.,

$$\tilde{x}(t) = x(t_k), t \in \{t_k + d_k + \tau_k^{sc}, k = 0, 1, 2, \ldots\}.$$

4) Using the above $\tilde{x}(t)$ and (4), the controller's output signal is obtained as

$$u(t) = Kx(t_k), t \in \{t_k + d_k + \tau_k^{sc}, k = 0, 1, 2, \ldots\}.$$

5) The above controller's output signal $u(t)$ is transferred to the actuator with network-induced delay τ_k^{ca}, so the actuator receives $u(t)$ at the instant $t_k + d_k + \tau_k^{sc} + \tau_k^{ca}$, and the actuator's input signal is expressed by

$$\tilde{u}(t) = Kx(t_k), t \in \{t_k + d_k + \tau_k^{sc} + \tau_k^{ca}, k = 0, 1, 2, \ldots\}.$$

6) After the control signal is received by the actuator (i.e., the above actuator's input signal $\tilde{u}(t_k + d_k + \tau_k^{sc} + \tau_k^{ca})$), it is stored in the zero-order hold of the actuator. This control signal is operated to the plant by the actuator's output end. The actuator's output signal will be changed until the next control signal arrives (i.e., the next actuator's input signal $\tilde{u}(t_{k+1} + d_{k+1} + \tau_{k+1}^{sc} + \tau_{k+1}^{ca})$). It means that the effective operating duration of the control signal is $[t_k + d_k + \tau_k^{sc} + \tau_k^{ca}, t_{k+1} + d_{k+1} + \tau_{k+1}^{sc} + \tau_{k+1}^{ca})$. We have

$$v(t) = Kx(t_k) \tag{5}$$
$$t \in [t_k + d_k + \tau_k^{sc} + \tau_k^{ca}, t_{k+1} + d_{k+1} + \tau_{k+1}^{sc} + \tau_{k+1}^{ca}).$$

The above analysis clearly shows that the controller creates the control signals after having received four-dimensional state information and enables the actuator to achieve the closed-loop control of the IPSs. Next, the characteristics of the above mentioned network-induced delay τ_k^{sc}, τ_k^{ca} and image processing time d_k are analyzed.

Considering the image processing time used for (1) and the bound of the network-induced delay [27], we shall have:

$$0 < \underline{d} \leqslant d_k \leqslant \bar{d}$$
$$0 \leqslant \tau_k^{sc} \leqslant \bar{\tau}_{sc}, 0 \leqslant \tau_k^{ca} \leqslant \bar{\tau}_{ca} \tag{6}$$

where $\bar{\tau}_{sc}$ and $\bar{\tau}_{ca}$ are the upper bounds of τ_k^{sc} and τ_k^{ca}, respectively.

The image sampling time t_k is related to the image processing time d_k due to the industrial camera using an event-triggered mechanism. In order to build the relationship between the sampling time t_k, the image processing time d_k, the network-induced delay τ_k^{sc}, τ_k^{ca} and the actuator execution time t, we reconsider the sampling instant t_k as

$$t_k = t - (t - t_k) = t - d(t) - \tau(t)$$
$$t \in [t_k + d_k + \tau_k^{sc} + \tau_k^{ca}, t_{k+1} + d_{k+1} + \tau_{k+1}^{sc} + \tau_{k+1}^{ca}) \tag{7}$$

where $d(t)$ is the image-induced computational delay, which is induced by the image processing time, and $\tau(t)$ is the total network-induced delay including τ_k^{sc} and τ_k^{ca}.

The time-varying delay $d(t)$ and $\tau(t)$ are bounded by

$$\mathcal{D}_1 \leqslant d(t) \leqslant \mathcal{D}_2, 0 \leqslant \tau(t) \leqslant \tau \tag{8}$$

where

$$\mathcal{D}_1 = \min_{k \in N}(d_k) = \underline{d}, \mathcal{D}_2 = \max_{k \in N}(d_k + d_{k+1}) = 2\bar{d}$$
$$\tau = \max_{k \in N}(\tau_{k+1}^{sc} + \tau_{k+1}^{ca}) = \bar{\tau}_{sc} + \bar{\tau}_{ca}.$$

Note that (8) demonstrates that the relationship between the upper bound of image-induced computational delay and the upper bound of the image processing time.

In case there is no data packet disorder, taking the derivatives of (7) with respect to t, the derivatives sum of $d(t)$ and $\tau(t)$ is

$$\dot{d}(t) + \dot{\tau}(t) = 1. \tag{9}$$

Assuming that $\dot{d}(t) = \mu_1 > 0, \dot{\tau}(t) = \mu_2 > 0$, then we have

$$\mu_1 + \mu_2 = 1. \tag{10}$$

Substituting (5) and (7) into (3) and considering computational errors $B_w w(t)$ lead to

$$\dot{x}(t) = Ax(t) + BKx(t - d(t) - \tau(t)) + B_w w(t)$$
$$z(t) = Cx(t) + DKx(t - d(t) - \tau(t)) \tag{11}$$
$$t \in [t_k + d_k + \tau_k^{sc} + \tau_k^{ca}, t_{k+1} + d_{k+1} + \tau_{k+1}^{sc} + \tau_{k+1}^{ca}).$$

It can be observed that the closed-loop system (11) is a continuous-time system with multiple time-varying delays and image processing computational errors.

As a special case of the closed-loop system (11), assuming that the external disturbance is absent ($w(t) = 0$), it takes no account of the influence of the image processing computational errors on the performance of the inverted pendulum. The closed-loop system (11) can be described as

$$\dot{x}(t) = Ax(t) + BKx(t - d(t) - \tau(t))$$
$$t \in [t_k + d_k + \tau_k^{sc} + \tau_k^{ca}, t_{k+1} + d_{k+1} + \tau_{k+1}^{sc} + \tau_{k+1}^{ca}). \tag{12}$$

Remark 6: Unlike the previous works [22], [23], the closed-loop system (11) is an intelligent system, which considers both image-induced computational and network-induced delays. Furthermore, it also takes into account the influence of computational errors caused by different system components, which is nearly ignored in the other approaches.

Remark 7: The closed-loop system (11) is with multiple time-varying delays, and the natures of various time-delay are different: $d(t)$ is related to the image processing time d_k and $\tau(t)$ is related to network-induced delay τ_k^{sc} and τ_k^{ca}. For this reason, two different delays cannot be simply added together and regarded as one single figure as treated in [31]–[34], without fully studying the respective characteristics of these two kinds of delays. In this paper, they are described as two kinds of time-varying delay so that we can explore the influence on the stability performance of the IPS.

C. Control Objectives

The problem to be addressed in this paper is formulated as follows.

H_∞ Control Problem [47], [48]: Given a scalar $\gamma > 0$, the closed-loop system (11) is said to be stabilizable with an H_∞-norm bound γ if there exists a state-feedback controller (5) such that two conditions are satisfied.

(1) The closed-loop system (11) is asymptotically stable when $w(t) = 0$;
(2) For any nonzero $w(t) \in \mathcal{L}_2(0, \infty)$,

$$\|z(t)\|_2 < \gamma \|w(t)\|_2 \tag{13}$$

is satisfied under zero initial conditions.

Remark 8: The computational errors of the state variables are denoted as (2). In this paper, the inequality (13), i.e., $\frac{\|z(t)\|_2}{\|w(t)\|_2} < \gamma$, is used to evaluate the disturbance attenuation ability. The smaller γ means the stronger disturbance attenuation ability.

IV. STABILITY ANALYSIS AND H_∞ CONTROLLER DESIGN

A. Stability Analysis

In this section, we will present sufficient conditions to solve the problem formulated in Section III. Firstly, we present one lemma below, which forms the foundation for deriving the major theorem.

Lemma 1 [49]: For any constant matrix $R \in \Re^{n \times n}$, $R = R^T > 0$, scalar $\mathcal{D}_1 \leqslant d(t) \leqslant \mathcal{D}_2$, and vector function $\dot{x} : [-\mathcal{D}_2, -\mathcal{D}_1] \to \Re^n$ such that the following integration is well defined, then

$$-(\mathcal{D}_2 - \mathcal{D}_1) \int_{t-\mathcal{D}_2}^{t-\mathcal{D}_1} \dot{x}^T(w) R \dot{x}(w) \, dw \leqslant H^T(t) \Omega H(t). \tag{14}$$

where

$$H(t) = \begin{bmatrix} x(t-\mathcal{D}_1) \\ x(t-d(t)) \\ x(t-\mathcal{D}_2) \end{bmatrix}, \qquad \Omega = \begin{bmatrix} -R & R & 0 \\ * & -2R & R \\ * & * & -R \end{bmatrix}.$$

Remark 9: The above Lemma 1 can be obtained by using Jensen's inequality [50]. If a different integral inequality is used (e.g., the canonical Bessel-Legendre inequality [51], the improved reciprocally convex inequality [52]), rather than Jensen's inequality, Lemma 1 can be replaced. However, the computation complexity will be higher because more decision variables are required. This new study will be carried out in the future.

Theorem 1: For some given constants $0 < \tau$, $0 < \mathcal{D}_1 < \mathcal{D}_2$, $\gamma > 0$ and $\mu_1 > 0$, $\mu_2 > 0$, if there exist real symmetric matrices $P > 0$, $Q_i > 0 \, (i = 1, 2, \ldots, 7)$, $Z_j > 0 \, (j = 1, 2, 3, 4)$ with appropriate dimensions, such that

$$\begin{bmatrix} \Pi_{11} & \Pi_{12} \\ * & \Pi_{22} \end{bmatrix} < 0 \tag{15}$$

hold, where $\Pi_{11} = \begin{bmatrix} \Pi_{11}^{11} & \Pi_{11}^{12} \\ * & \Pi_{11}^{22} \end{bmatrix}$ and

$\Pi_{11}^{11} =$
$$\begin{bmatrix} \Psi_{11} & Z_1 & 0 & 0 & Z_3 & 0 & PBK & 0 \\ * & \Psi_{22} & Z_2 & 0 & 0 & 0 & Z_4 & 0 \\ * & * & \Psi_{33} & Z_2 & 0 & 0 & 0 & 0 \\ * & * & * & \Psi_{44} & 0 & 0 & 0 & 0 \\ * & * & * & * & \Psi_{55} & Z_3 & 0 & 0 \\ * & * & * & * & * & \Psi_{66} & 0 & 0 \\ * & * & * & * & * & * & \Psi_{77} & Z_4 \\ * & * & * & * & * & * & * & \Psi_{88} \end{bmatrix}$$

$\Pi_{11}^{12} = \begin{bmatrix} B_w P & E_1 \otimes 0 & 0 & 0 \\ C & E_1 \otimes 0 & DK & 0 \end{bmatrix}^T$

$\Pi_{11}^{22} = diag \{-\gamma^2 I, -I\}$

$\Psi_{11} = PA + A^T P + \sum_{i=1}^{7} Q_i - Z_1 - Z_3$

$\Psi_{22} = -Q_1 - Z_1 - Z_2 - Z_4$

$\Psi_{33} = -(1 - \mu_1) Q_2 - 2Z_2$

$\Psi_{44} = -Q_3 - Z_2$

$\Psi_{55} = -(1 - \mu_2) Q_4 - 2Z_3$

$\Psi_{66} = -Q_5 - Z_3$

$\Psi_{77} = -2Z_4$

$\Psi_{88} = -Q_7 - Z_4$

$\Pi_{12} =$

$\begin{bmatrix} \hat{Z}^T A\Lambda^T, E_2^T \otimes 0, \hat{Z}^T BK\Lambda^T, E_3^T \otimes 0, \hat{Z}^T B_w, E_3^T \otimes 0 \end{bmatrix}^T$

$\Pi_{22} = -diag \{Z_1, Z_2, Z_3, Z_4\}$,

$\hat{Z} = \begin{bmatrix} Z_1^T & Z_2^T & Z_3^T & Z_4^T \end{bmatrix}^T$

$\Lambda = diag \{\mathcal{D}_1 I, \mathcal{D}_{12} I, \tau I, \mathcal{D}_{13} I\}$

$E_1 = [E_3, 1]$

$E_2 = \begin{bmatrix} E_3^T, E_3^T, E_3^T, E_3^T \end{bmatrix}^T$

$E_3 = \begin{bmatrix} 1 & 1 & 1 & 1 \end{bmatrix}$

$\mathcal{D}_{12} = \mathcal{D}_2 - \mathcal{D}_1$, $\mathcal{D}_{13} = \mathcal{D}_3 - \mathcal{D}_1$, $\mathcal{D}_3 = \mathcal{D}_2 + \tau$

then the closed-loop system (11) is asymptotically stable with an H_∞ disturbance attenuation level γ under zero initial condition for all the time-delay satisfying (8)-(10).

Proof: See Appendix A.

Remark 10: A linear matrix inequality (LMI) for the H_∞ control problem similar to (15) is considered in [53] in the context of disturbance attenuation for time-delay systems. The difference lies in two aspects: 1) The disturbance is caused by computational errors of image processing in additional to noise. 2) The time-varying delays include both network-induced delay and image-induced computational delay. Using Theorem 1, the stability of the closed-loop system (11) with multiple time-varying delays and external disturbance is proved, which reflects the relationship between image-induced computational and network-induced issues and system performance. This work has important significance for the CPS with the 3C concerns.

Corollary 1: For some given constants $0 < \tau$, $0 < \mathcal{D}_1 < \mathcal{D}_2$ and $\mu_1 > 0$, $\mu_2 > 0$, if there exist real symmetric matrices $P > 0$, $Q_i > 0 \, (i = 1, 2, \ldots, 7)$, $Z_j > 0 \, (j = 1, 2, 3, 4)$ with appropriate dimensions, such that

$$\begin{bmatrix} \bar{\Pi}_{11} & \bar{\Pi}_{12} \\ * & \bar{\Pi}_{22} \end{bmatrix} < 0 \tag{16}$$

hold, where

$\bar{\Pi}_{11} = \Pi_{11}^{11}$

$\bar{\Pi}_{12} = \begin{bmatrix} Z^T A\Lambda^T, E_2^T \otimes 0, Z^T BK\Lambda^T, E_3^T \otimes 0 \end{bmatrix}^T$

$\bar{\Pi}_{22} = \Pi_{22}$

then the closed-loop system (12) is asymptotically stable for all the time-delay satisfying (8)-(10).

Proof: The proof is similar to that of Theorem 1, which is omitted here.

B. H_∞ Controller Design

Deriving the feedback gain K in Theorem 1 involves nonlinear terms such as PBK in (15) that cannot be retrieved straightforward. However, the nonlinear terms can be eliminated using a spacial matrix $X = P^{-1}$ such that an LMI formulation is created. The controller design algorithm is given in the following theorem.

Theorem 2: For some given constants $0 < \tau$, $0 < \mathcal{D}_1 < \mathcal{D}_2$, $\gamma > 0$ and $\mu_1 > 0$, $\mu_2 > 0$, $\varepsilon_j \, (j = 1, 2, 3, 4)$, if there exist real symmetric matrices $X > 0$, $\tilde{Q}_i > 0 \, (i = 1, 2, \ldots, 7)$, $\tilde{Z}_j > 0 \, (j = 1, 2, 3, 4)$ and arbitrary matrix Y with appropriate dimensions, such that

$$\begin{bmatrix} \Phi_{11} & \Phi_{12} \\ * & \Phi_{22} \end{bmatrix} < 0 \tag{17}$$

hold, where $\Phi_{11} = \begin{bmatrix} \Phi_{11}^{11} & \Phi_{11}^{12} \\ * & \Phi_{11}^{22} \end{bmatrix}$ and

$\Phi_{11}^{11} =$

$$\begin{bmatrix} \Theta_{11} & \tilde{Z}_1 & 0 & 0 & \tilde{Z}_3 & 0 & BY & 0 \\ * & \Theta_{22} & \tilde{Z}_2 & 0 & 0 & 0 & \tilde{Z}_4 & 0 \\ * & * & \Theta_{33} & \tilde{Z}_2 & 0 & 0 & 0 & 0 \\ * & * & * & \Theta_{44} & 0 & 0 & 0 & 0 \\ * & * & * & * & \Theta_{55} & \tilde{Z}_3 & 0 & 0 \\ * & * & * & * & * & \Theta_{66} & 0 & 0 \\ * & * & * & * & * & * & \Theta_{77} & \tilde{Z}_4 \\ * & * & * & * & * & * & * & \Theta_{88} \end{bmatrix}$$

$\Phi_{11}^{12} = \begin{bmatrix} B_w & E_1 \otimes 0 & 0 & 0 \\ CX^T & E_1 \otimes 0 & DY & 0 \end{bmatrix}^T$

$\Phi_{11}^{22} = diag\left\{-\gamma^2 I, -I\right\}$

$\Phi_{12} =$

$\left[AX\Lambda^T, E_2^T \otimes 0, BY\Lambda^T, E_3^T \otimes 0, B_w^T \Lambda^T, E_3^T \otimes 0\right]^T$

$\Phi_{22} = -diag\left\{\Gamma_1, \Gamma_2, \Gamma_3, \Gamma_4\right\}$

$\Theta_{11} = AX + XA^T + \sum_{i=1}^{7} \tilde{Q}_i - \tilde{Z}_1 - \tilde{Z}_3$

$\Theta_{22} = -\tilde{Q}_1 - \tilde{Z}_1 - \tilde{Z}_2 - \tilde{Z}_4$

$\Theta_{33} = -\left(1 - \mu_1\right)\tilde{Q}_2 - 2\tilde{Z}_2$

$\Theta_{44} = -\tilde{Q}_3 - \tilde{Z}_2$

$\Theta_{55} = -\left(1 - \mu_2\right)\tilde{Q}_4 - 2\tilde{Z}_3$

$\Theta_{66} = -\tilde{Q}_5 - \tilde{Z}_3$

$\Theta_{77} = -2\tilde{Z}_4$

$\Theta_{88} = -\tilde{Q}_7 - \tilde{Z}_4$

$\Gamma_j = -2\varepsilon_j X + \varepsilon_j^2 \tilde{Z}_j \ (j = 1, 2, 3, 4)$

and Λ, E_1, E_2, E_3, $\mathcal{D}_{12}$, $\mathcal{D}_{13}$, $\mathcal{D}_3$ are defined in Theorem 1, then the closed-loop system (11) is asymptotically stable with an H_∞ disturbance attenuation level γ under zero initial condition for all the time-delay satisfying (8)-(10), with a state feedback gain $K = YX^{-1}$.

Proof: See Appendix B.

Remark 11: Given the parameters of multiple time-varying delays and H_∞ disturbance attenuation level γ, the state feedback gain K can be obtained by solving (17).

Corollary 2: For some given constants $0 < \tau$, $0 < \mathcal{D}_1 < \mathcal{D}_2$ and $\mu_1 > 0$, $\mu_2 > 0$, $\varepsilon_j \ (j = 1, 2, 3, 4)$, if there exist real symmetric matrices $X > 0$, $\tilde{Q}_i > 0 \ (i = 1, 2, \ldots, 7)$, $\tilde{Z}_j > 0 \ (j = 1, 2, 3, 4)$ and arbitrary matrix Y with appropriate dimensions, such that

$$\begin{bmatrix} \bar{\Phi}_{11} & \bar{\Phi}_{12} \\ * & \bar{\Phi}_{22} \end{bmatrix} < 0 \qquad (18)$$

hold, where

$\bar{\Phi}_{11} = \Phi_{11}^{11}$

$\bar{\Phi}_{12} = \left[AX^T\Lambda^T, E_2^T \otimes 0, BY\Lambda^T, E_3^T \otimes 0\right]^T$

$\bar{\Phi}_{22} = \Phi_{22}$

then the closed-loop system (12) is asymptotically stable for all the time-delay satisfying (8)-(10), with a state feedback gain $K = YX^{-1}$.

Proof: The proof is similar to that of Theorem 2, which is omitted here.
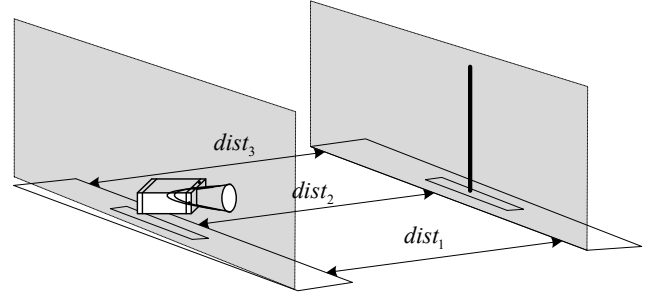

Fig. 3. The plane of the inverted pendulum is parallel to that of the camera.

V. EXPERIMENTS

A. Building the Experimental Platform

In this paper, a new IPS named NIPVSS is presented in Section III of the supplementary materials. However, two reasons contribute to the instability of the IPS.

1) Computational errors: These errors mainly come from two factors: i) The images of the inverted pendulum are affected by the experimental environments, such as illumination, background, etc. ii) Due to the distance between the image plane and the inverted pendulum plane, we have to resize the acquired images collected by the platform as shown in Fig. 3. All of these factors will amplify the computational errors and affect the stability of the control system.

2) Image processing time: It is time-consuming to locate feature points in the cart and pendulum images. Meanwhile, according to the pixel displacement of the feature points, the pendulum angles and the cart positions are computed using the standard inverse triangular function method [54], which inevitably increases the computational time of the system, affecting the selection of the control cycles and the control performance of the NIPVSS.

We solve them as follows:

1) To reduce the influence of illumination, background and external uncertainty on image acquisition and processing, five light-emitting diode (LED) stroboscopic fluorescent lamps with adjustable illumination levels are used as the light sources, which are erected vertically above the inverted pendulum platform. This ensures uniform illumination to correspond to the motion range of the inverted pendulum.

2) To reduce the errors caused by the non-parallel planes between the inverted pendulum and the camera, we use a level meter to ensure the horizontal placement of their individual platforms, and then the shortest distance between two planes is measured by selecting three points located on left, middle and right hand side of the inverted pendulum. We let $dist_1 = dist_2 = dist_3$ to ensure that the two planes are parallel to each other, as shown in Fig. 3.

Considering image-induced computational delay and errors mentioned above, the experimental environment, hardware platform and system model are fixed and an ultimate NIPVSS is shown in Fig. 4.

Fig. 4. Experimental platform of the NIPVSS.

Fig. 5. Cart positions with controller gain K_1 (simulation and experiment) and controller gain K_2 (simulation)

Fig. 6. Pendulum angles with controller gain K_1 (simulation and experiment) and controller gain K_2 (simulation)

Remark 12: Note that compared with the traditional inverted pendulum experiment platforms [55], [56], the application of visual sensing will inevitably lead to the problems of illumination and the image plane nonparallel to the main inverted pendulum plane. We solve these problems using five LED stroboscopic fluorescent lamps with adjustable illumination levels as the light sources and a level meter. Indeed, the final NIPVSS developed in this project includes: (1) GLIP2001C linear motion inverted pendulum produced by Gu Hi-Tech Ltd. (2) Aca640-120gm monochrome camera with light sources. (3) The controller contains a PC, GT-400-SV motion control card and MSMA023A1A AC servo motor driver, which is used to drive the cart-inverted pendulum.

B. Simulation and Real-time Control Experiments

In the above section, the stability of the NIPVSS with multiple time-varying delays and computational errors have been analyzed, and the stability performance indicator and the working conditions of the controller are presented as well. In this section, to validate the effectiveness and real-time performance of the proposed method, simulations and real-time control procedure are demonstrated. The design of the controller are based on Theorem 2 and Corollary 2 presented in section IV. In order to apply Theorem 2 and Corollary 2, it is necessary to know the parameters, i.e., the low and upper bounds ($\mathcal{D}_1$ and $\mathcal{D}_2$) of time-varying $d(t)$, the upper bound (τ) of the time-varying $\tau(t)$, H_∞ disturbance attenuation level γ, and $\mu_1, \mu_2, \varepsilon_j \, (j = 1, 2, 3, 4)$. From (1), (6) and (8), we know that

$$\mathcal{D}_1 = \min_{k \in N}(d_k) = 0.019s, \mathcal{D}_2 = \max_{k \in N}(d_k + d_{k+1}) = 0.058s.$$

Moreover, it is noticed that $\tau_k^{sc} \in (0, 0.007]\,s$ and $\tau_k^{ca} \in (0, 0.007]\,s$. Empirical evidence shows $\bar{\tau}_{sc} = 0.007s$ and $\bar{\tau}_{ca} = 0.007s$. From (8), we can derive that

$$\tau = \max_{k \in N}\left(\tau_{k+1}^{sc} + \tau_{k+1}^{ca}\right) = \bar{\tau}_{sc} + \bar{\tau}_{ca} = 0.014s.$$
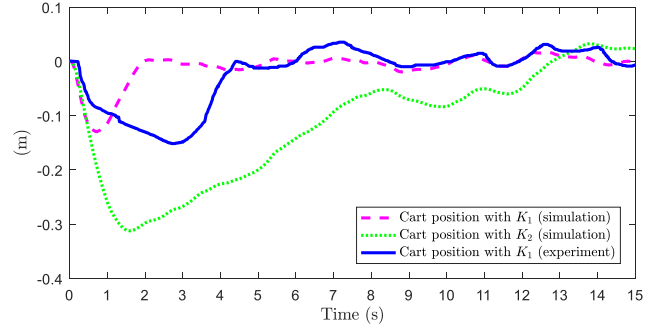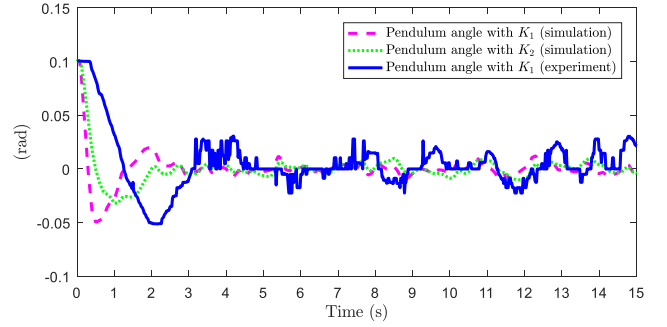
Other parameters γ, μ_1, μ_2 and $\varepsilon_j \, (j = 1, 2, 3, 4)$ are given as follows:

$$\gamma = 2.1, \mu_1 = 0.3, \mu_2 = 0.7$$
$$\varepsilon_1 = 0.01, \varepsilon_2 = 0.75, \varepsilon_3 = 1.2, \varepsilon_4 = 0.022.$$

The parameters γ and $\varepsilon_j \, (j = 1, 2, 3, 4)$ have been chosen heuristically as they satisfy Theorem 2 and the controllers. For μ_1 and μ_2, according to the statistical characteristics of $\dot{\tau}(t)$, the mean value of $\dot{\tau}(t)$ is firstly calculated as 0.6791, so μ_2 is approximately set as 0.7. Then, according to (10), μ_1 is set as 0.3.

Then, after having solved (17) and (18), we get the controller gain K_1 of the closed-loop system (11) and the controller gain K_2 of the closed-loop system (12) which are shown as follows:

$$K_1 = \left[\begin{array}{cccc} 3.7137 & -29.3065 & 4.0140 & -5.3880 \end{array}\right]$$
$$K_2 = \left[\begin{array}{cccc} 0.1866 & -18.8363 & 0.7655 & -3.4738 \end{array}\right].$$

We now verify the rationality and validity of the proposed method from 4 aspects.

1) Analyzing the influence of computational errors on the inverted pendulum system's performance.

The experimental platform of the NIPVSS is shown in Fig. 4. In order to analyze the influence of computational errors on the IPS performance and evaluate the performance of the controller through Theorem 2 and Corollary 2, simulations and real-time experiments have been implemented to compare the performance of controllers K_1 and K_2. The initial conditions of the state quantity are set to be $x_0 = \left[\begin{array}{cccc} 0 & 0.100 & 0 & 0 \end{array}\right]^T$.

The simulation and experimental results are shown in Figs. 5 and 6. They illustrate the cart positions and the pendulum angles with the controller gain K_1 (simulation and experiment, considering the image processing errors) and under controller gain K_2 (simulation, ignoring computational errors), respectively. We will firstly consider the simulation results. Comparing Figs. 5 and 6, we notice that the cart and the pendulum soon move into a stable state with small fluctuations with the controller gain K_1, although the cart and the pendulum can move into a stable state with the controller gain K_2 where the cart traverses on the rail with large offsets. The control performance with the controller gain K_1 is obviously better than that with the controller gain K_2.

Then, the real-time control experiments are conducted on building the experimental platform with different controller gains K_1 and K_2, respectively. Network-induced delay is randomly produced according to the measures $(0, 0.014] \, s$. The experiments verify that the controller gain K_1 results in stable control of the cart-inverted pendulum and the real-time control result is illustrated in Figs. 5 and 6, which show that the cart and the pendulum soon move into a stable state with a relatively stable performance. However, the controller gain K_2 is unable to achieve the stable control of the cart-inverted pendulum. These indicate that it is reasonably necessary to consider the influence of computational errors on the NIPVSS performance.

Analyzing the outcomes shown in Figs. 5 and 6 with the same controller gain K_1, we observe a minor discrepancy between the simulation and experiment results. Two possible reasons attribute to this: (1) The linearized IPS is not accurate. (2) The delay and errors may be due to data transaction between system components which is beyond the current discuss.

2) Analyzing the relationship between network-induced delay and image-induced computational delay.

TABLE II
GIVEN THE UPPER BOUND τ OF NETWORK-INDUCED DELAY, THE UPPER BOUND $\mathcal{D}_2$ OF IMAGE-INDUCED COMPUTATIONAL DELAY AND THE UPPER BOUND $\bar{d}$ OF THE IMAGE PROCESSING TIME.

Given τ	0	0.01	0.02	0.04	0.06	0.08	0.084
$\mathcal{D}_2$	0.086	0.076	0.066	0.046	0.026	0.006	0
$\bar{d}$	0.043	0.038	0.033	0.023	0.013	0.003	0

The relationship, for the IPS stability performance, between network-induced and computational delays needs to be analyzed according to Theorem 1 with the controller gain K_1. Given the upper bound τ of network-induced delay, we infer the upper bound $\mathcal{D}_2$ of the time-varying image-induced computational delay, i.e., the upper bound $\bar{d}$ of the image processing time which ensures the closed-loop system (11) to be stable and controllable according to Theorem 1, and vice versa. The corresponding linear relationships between τ, $\mathcal{D}_2$ and $\bar{d}$ are listed in Table II. Table II depicts that the theoretical variation ranges of network-induced delay and image processing time are $\tau(t) \in (0, 0.084] \, s$ and $\bar{d} \in [0, 0.043] \, s$, respectively. As a comparison, the experimental variation ranges of the
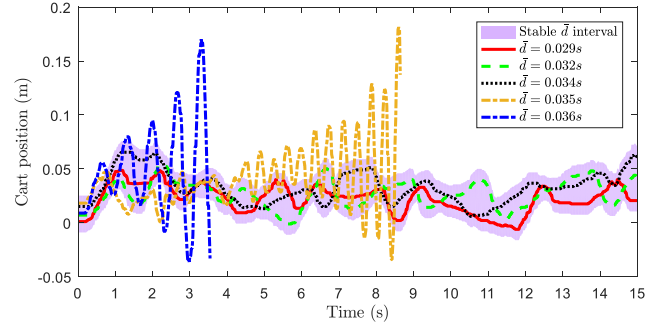

Fig. 7. Cart positions with different upper bounds $\bar{d}$ of image processing time.
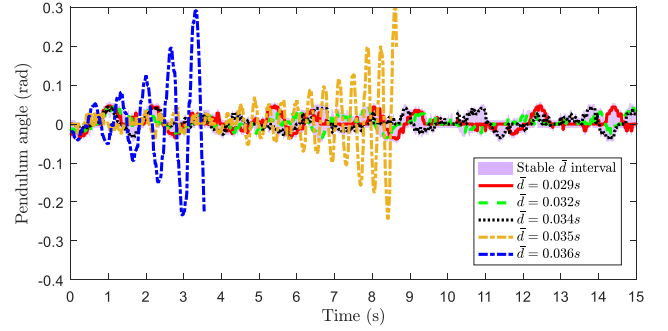

Fig. 8. pendulum angles with different upper bounds $\bar{d}$ of image processing time.

network-induced delay and image processing time in this paper respectively are $\tau(t) \in (0, 0.014] \, s$ and $\bar{d} \in [0.019, 0.029] \, s$. In result, the experimental variation ranges is a subset of the theoretical ones. These verify the effectiveness of the proposed method.

3) Analyzing the influence of image-induced computational delay on the inverted pendulum system's performance.

The maximum upper bound of the time-varying image-induced computational delay is $\mathcal{D}_2 = 0.072s$ (i.e., the maximum upper bound of the image processing time is $\bar{d} = 0.036s$) which ensures the closed-loop system (11) stable and controllable according to Theorem 1 with the variation range $\tau(t) \in (0, 0.014] \, s$ of network-induced delay with the controller gain K_1. When $\mathcal{D}_2 > 0.072s$ (i.e., $\bar{d} > 0.036s$), the closed-loop system (11) is divergent and uncontrolled which indicates that the influence of image-induced computational delay on the control system performance is relatively strong. In order to analyze the actual influence of image-induced computational delay on the inverted pendulum system performance, the real-time control experiments are subsequently implemented with different upper bounds of the image processing time $\bar{d} = 0.029s/0.032s/0.034s/0.035s/0.036s$, respectively, and the initial conditions of the status quantity have been set as $x_0 = \begin{bmatrix} 0 & 0 & 0 & 0 \end{bmatrix}^T$. The cart positions and the pendulum angles of the real-time control experiments are illustrated in Figs. 7 and 8, respectively. Furthermore, the mean and standard deviation (STD) of the cart positions and pendulum angles are used to show the stable performance of the inverted pendulum system. The mean of the cart positions displays the extent of the cart deviating from the initial position and that of
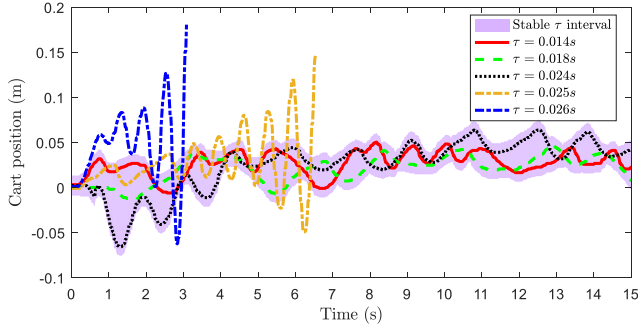
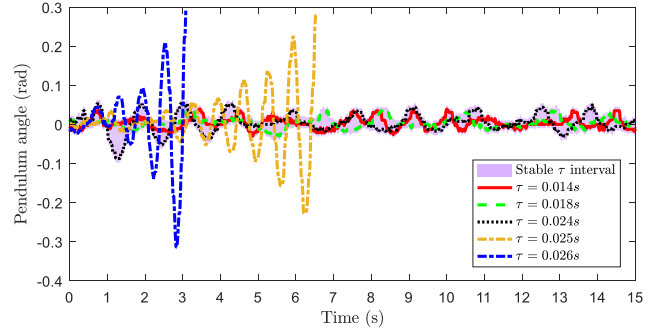Fig. 9. Cart positions with different upper bounds τ of the network-induced delay.

Fig. 10. Pendulum angles with different upper bounds τ of the network-induced delay.

the pendulum angles displays the degree of the pendulum deviating from the vertical direction. The STD of the cart positions and pendulum angles displays the extent of the cart and the pendulum deviating from the mean, i.e., the fluctuation degree of the cart and the pendulum. The mean and STD of the cart positions and pendulum angles are illustrated in Table III, respectively.

TABLE III
MEAN AND STD OF CART POSITIONS AND PENDULUM ANGLES UNDER DIFFERENT UPPER BOUNDS $\bar{d}$ OF THE IMAGE PROCESSING COMPUTATIONAL TIME.

	$\bar{d}$				
	0.029	0.032	**0.034**	0.035	0.036
MCP[1](m)	0.0226	0.0288	**0.0315**	0.0397	0.0479
SCP[2](m)	0.0349	0.0446	**0.0487**	0.0692	0.0913
MPA[3](rad)	0.0039	0.0035	**0.0035**	0.0064	0.0062
SPA[4](rad)	0.0202	0.0211	**0.0237**	0.0716	0.1145

[1] Mean of cart position. [2] STD of cart position.
[3] Mean of pendulum angle. [4] STD of pendulum angle.

Table III shows that, when the image processing time is $\bar{d} = 0.029s/0.032s/0.034s$, the curves of the cart positions and pendulum angles have no significant difference and the fluctuations of these curves slightly increase with gradually increasing $\bar{d}$. When the image processing time is $\bar{d} = 0.035s/0.036s$, the curves of the cart positions and pendulum angles show large fluctuations. Table III shows that, when the image processing time is $\bar{d} \leqslant 0.034s$, the mean and STD of the cart positions and pendulum angles slightly increase with gradually increasing $\bar{d}$. when the image processing time is $\bar{d} > 0.034s$, the STD of the cart positions and pendulum angles appear to be of large increase, i.e., the dispersion degree of the cart positions and pendulum angles rapidly increase. Figs. 7 and 8 and Table III show that, within a certain change range of image processing time, the designed controller is able to achieve stable control on the cart-inverted pendulum and the stability performance slightly deteriorates with gradually increasing image processing time. When the image processing time exceeds a certain limit, the designed controller is unable to achieve stable control of the cart-inverted pendulum. The allowable maximum upper bound of the image processing time ($\bar{d} = 0.034s$), which ensures the cart-inverted pendulum stable and controllable, is slightly less than the theoretical derivation threshold ($\bar{d} = 0.036s$). Due to the uncontrollable experi-

mental environment, the theoretical simulation is unable to simulate the actual conditions, resulting in that the theoretical threshold is larger than the actual result. The experimental results show that image-induced computational delay (i.e., it is induced by the image processing time) has a significant influence on the performance of the inverted pendulum system and efficient image processing algorithms are required to improve the image processing speed whilst reducing image processing time.

4) Analyzing the influence of network-induced delay on the inverted pendulum system's performance.

TABLE IV
MEAN AND STD OF THE CART POSITIONS AND PENDULUM ANGLES IN DIFFERENT UPPER BOUNDS τ OF THE IMAGE PROCESSING TIME.

	τ				
	0.0140	0.0180	**0.0240**	0.0250	0.0260
MCP[1](m)	0.0240	0.0280	**0.0310**	0.0380	0.0450
SCP[2](m)	0.0370	0.0430	**0.0500**	0.0690	0.0870
MPA[3](rad)	0.0029	0.0037	**0.0041**	0.0041	0.0051
SPA[4](rad)	0.0162	0.0183	**0.0219**	0.0781	0.1057

[1] Mean of cart position. [2] STD of cart position.
[3] Mean of pendulum angle. [4] STD of pendulum angle.

The maximum upper bound of the time-varying network-induced delay is $\tau = 0.028s$, which ensures the closed-loop system (11) stable and controllable with the variation range $\mathcal{D}_2 \in [0.019, 0.058]\,s$ of the time-varying computational delay and controller gain K_1. When $\tau > 0.028s$, the closed-loop system (11) is divergent and uncontrolled which indicates that the influence of network-induced delay on the control system performance is significant. In order to analyze the actual influence of network-induced delay on the inverted pendulum system's performance, the real-time control experiments are subsequently implemented with the upper bound of network-induced delay $\tau = 0.014s/0.018s/0.024s/0.025s/0.026s$, respectively, and the initial conditions of the status quantity have been set to be $x_0 = \begin{bmatrix} 0 & 0 & 0 & 0 \end{bmatrix}^T$. The cart positions and pendulum angles of the real-time control experiments are illustrated in Figs. 9 and 10, respectively. Furthermore, the mean and standard deviation (STD) of the cart positions and pendulum angles are also used to show the stability performance of the inverted pendulum system and the mean and STD of the cart positions and pendulum angles are

illustrated in Table IV, respectively.

Figs. 9 and 10 show that, when network-induced delay is $\tau = 0.014s/0.018s/0.024s$, the curves of the cart positions and pendulum angles have no significant difference and the fluctuations of these curves slightly increase with gradual increasing τ. When network-induced delay is $\tau = 0.025s/0.026s$, the curves of the cart positions and pendulum angles show large fluctuations. Table IV shows that, when network-induced delay is $\tau \leqslant 0.024s$, the mean and STD of cart positions and pendulum angles slightly increase without significant increase with gradually increasing τ; When network-induced delay is $\tau > 0.034s$, the STD of the cart positions and pendulum angles have significant increases, i.e., the dispersion degrees of the cart positions and pendulum angles rapidly increase. Figs. 9 and 10 and Table IV all show that, within a certain change range of network-induced delay, the designed controller is able to achieve stable control towards the cart-inverted pendulum and the stability performance slightly deteriorates with gradually increasing image processing time. When network-induced delay exceeds a certain threshold, the designed controller is unable to achieve stable control on the cart-inverted pendulum. We observe that the allowable maximum upper bound of the network-induced delay ($\tau = 0.024s$), which ensures the cart-inverted pendulum stable and controllable, is slightly less than the theoretical expectation ($\tau = 0.028s$). Since the actual experimental environment is complex and multiple factors influence the stability performance of the inverted pendulum, the theoretical simulation is unable to simulate the actual conditions and the theoretical threshold is greater than the actual measurement. The results of the experiments show that network-induced delay has a significant influence on the inverted pendulum system's performance, and the network transmission rate and transmission quality need to be improved to reduce network-induced delay.

VI. CONCLUSION

The objective of this paper is to solve the real-time control problem of a networked inverted pendulum visual servo system, which jointly involves communication networking and visual servo. An experimental platform of the networked inverted pendulum visual servo control has been designed and fully investigated. The characteristics of image processing time and computational errors are then analyzed based on a large amount of experiments whilst the event-triggered sampling mechanism of visual sensors is designed. Furthermore, a new closed-loop model of the networked inverted pendulum visual servo system with multiple time-varying delays and computational errors are established considering the different characteristics of image-induced computational and network-induced delays. Moreover, an H_∞ disturbance attenuation level γ was given, and the corresponding H_∞ controller design has been accomplished using the linear matrix inequality approach. Finally, the simulation and real-time control experimental results demonstrated the effectiveness of the proposed design method. In the future, using some filtering methods such as [57], the filtering of signals for the NIPVSS are very interesting and significant research venues.

APPENDIX A
PROOF OF THEOREM 1

Define a Lyapunov functional as

$$V(x(t)) = V_1 + V_2 + V_3 + V_4 + V_5 + V_6 + V_7 \qquad (19)$$

where
$V_1 = x^T(t) P x(t)$
$V_2 = \int_{t-\mathcal{D}_1}^{t} x^T(s) Q_1 x(s) ds$
$\quad + \int_{t-d(t)}^{t} x^T(s) Q_2 x(s) ds + \int_{t-\mathcal{D}_2}^{t} x^T(s) Q_3 x(s) ds$
$V_3 = \int_{-\mathcal{D}_1}^{0} \int_{t+\theta}^{t} \mathcal{D}_1 \dot{x}^T(s) Z_1 \dot{x}(s) ds d\theta$
$\quad + \int_{-\mathcal{D}_2}^{-\mathcal{D}_1} \int_{t+\theta}^{t} \mathcal{D}_{12} \dot{x}^T(s) Z_2 \dot{x}(s) ds d\theta$
$V_4 = \int_{t-\tau(t)}^{t} x^T(s) Q_4 x(s) ds + \int_{t-\tau}^{t} x^T(s) Q_5 x(s) ds$
$V_5 = \int_{-\tau}^{0} \int_{t+\theta}^{t} \tau \dot{x}^T(s) Z_3 \dot{x}(s) ds d\theta$
$V_6 = \int_{t-d(t)-\tau(t)}^{t} x^T(s) Q_6 x(s) ds + \int_{t-\mathcal{D}_3}^{t} x^T(s) Q_7 x(s) ds$
$V_7 = \int_{-\mathcal{D}_3}^{-\mathcal{D}_1} \int_{t+\theta}^{t} \mathcal{D}_{13} \dot{x}^T(s) Z_4 \dot{x}(s) ds d\theta.$

Then, taking the derivative of $V(x(t))$ with respect to t and using Jensen's inequality and Lemma 1 lead to

$$\dot{V}(x(t)) \leqslant \zeta^T(t) \Omega \zeta(t) + \gamma^2 w^T(t) w(t) \qquad (20)$$

where

$\zeta^T(t) = [x^T(t) \quad x^T(t-\mathcal{D}_1) \quad x^T(t-d(t))$
$x^T(t-\mathcal{D}_2) \quad x^T(t-\tau(t)) \quad x^T(t-\tau) \quad x^T(t-d(t)-\tau(t))$
$x^T(t-\mathcal{D}_3) \quad w(t)]$

$$\Omega = \begin{bmatrix} \Omega_{11} & \Omega_{12} \\ * & \Omega_{22} \end{bmatrix}$$

$$\Omega_{11} = \begin{bmatrix} \Xi_{11} & Z_1 & 0 & 0 \\ * & \Xi_{22} & Z_2 & 0 \\ * & * & \Xi_{33} & Z_2 \\ * & * & * & \Xi_{44} \end{bmatrix}$$

$$\Omega_{12} = \begin{bmatrix} Z_3 & 0 & \Xi_{17} & 0 & \Xi_{19} \\ 0 & 0 & Z_4 & 0 & 0 \\ 0 & 0 & 0 & 0 & 0 \\ 0 & 0 & 0 & 0 & 0 \end{bmatrix}$$

$$\Omega_{22} = \begin{bmatrix} \Xi_{55} & Z_3 & 0 & 0 & 0 \\ * & \Xi_{66} & 0 & 0 & 0 \\ * & * & \Xi_{77} & Z_4 & \Xi_{79} \\ * & * & * & \Xi_{88} & 0 \\ * & * & * & * & \Xi_{99} \end{bmatrix}$$

$\Xi_{11} = PA + A^T P + \sum_{i=1}^{7} Q_i - Z_1 - Z_3 + A^T \bar{Z} A$
$\Xi_{22} = -Q_1 - Z_1 - Z_2 - Z_4$
$\Xi_{33} = -(1-\mu_1) Q_2 - 2Z_2$
$\Xi_{44} = -Q_3 - Z_2$
$\Xi_{55} = -(1-\mu_2) Q_4 - 2Z_3$
$\Xi_{66} = -Q_5 - Z_3$
$\Xi_{77} = -2Z_4 + K^T B^T \bar{Z} BK$
$\Xi_{88} = -Q_7 - Z_4$
$\Xi_{99} = -\gamma^2 I + B_w^T \bar{Z} B_w$
$\Xi_{17} = PBK + A^T \bar{Z} BK$
$\Xi_{19} = PB_w + A^T \bar{Z} B_w$

$\Xi_{79} = K^T B^T \bar{Z} B_w$

$\bar{Z} = \mathcal{D}_1^2 Z_1 + \mathcal{D}_{12}^2 Z_2 + \tau^2 Z_3 + \mathcal{D}_{13}^2 Z_4.$

Next, we will prove Theorem 1 from two aspects according to the problem formulated in Section III.

One Aspect: Assuming that $w(t) = 0$, if $\Omega < 0$, it follows that

$$\dot{V}(x(t)) \leqslant 0 \tag{21}$$

then the closed-loop system (11) is asymptotically stable in the absence of $w(t)$ for all time-delay satisfying (8)-(10).

Another Aspect: Any nonzero $w(t) \in \mathcal{L}_2(0, \infty)$. Adding $z^T(t)z(t)$ to the left and right sides of (20) and moving $\gamma^2 w^T(t) w(t)$ to the left side leads to

$$\dot{V}(x(t)) + z^T(t) z(t) - \gamma^2 w^T(t) w(t) \leqslant \zeta^T(t) \Gamma \zeta(t) \tag{22}$$

where $\Gamma = \begin{bmatrix} \Gamma_{11} & \Gamma_{12} \\ * & \Gamma_{22} \end{bmatrix}$ and

$\Gamma_{11} = \Omega_{11} + diag\{C^T C, 0, 0, 0\}$

$\Gamma_{12} = \Omega_{12} + \left[\bar{C}^T \otimes I, \bar{C}^T \otimes 0, \bar{C}^T \otimes 0, \bar{C}^T \otimes 0 \right]^T$

$\Gamma_{22} = \Omega_{22} + diag\{0, 0, K^T D^T DK, 0, 0\}$

$\bar{C} = [0, 0, C^T DK, 0, 0]$

and I is the identity matrix with an appropriate dimension. If $\Gamma < 0$ is established, it follows that

$$\dot{V}(x(t)) + z^T(t) z(t) - \gamma^2 w^T(t) w(t) < 0. \tag{23}$$

Under zero initial condition, i.e., $V(0) = 0$, the two sides are integrated from 0 to ∞, resulting in

$$\int_0^\infty \left[z^T(t)z(t) - \gamma^2 w^T(t)w(t) \right] dt \atop < V(0) - V(\infty) = -V(\infty) < 0 \tag{24}$$

which means that $\|z(t)\|_2 < \gamma \|w(t)\|_2$ is established.

According to the Schur complement, (15) is satisfied, inferring $\Gamma < 0$ and $\Omega < 0$. The proof is thus completed.

APPENDIX B
PROOF OF THEOREM 2

Pre- and post-multiplying the inequality (16) in section III with

$$diag\left\{ \underbrace{P^{-1}, \dots, P^{-1}}_{8}, I, I, \underbrace{Z_2^{-1}, \dots, Z_2^{-1}}_{4} \right\}$$

and its transpose, respectively, and setting

$$X = P^{-1}, \tilde{Q}_i = P^{-1} Q_i P^{-1} \ (i = 1, 2, \dots, 7)$$

$$\tilde{Z}_j = P^{-1} Z_j P^{-1} \ (j = 1, 2, \dots, 4), Y = KX.$$

Because $(\varepsilon X - R) R^{-1} (\varepsilon X - R) > 0$, where $R = R^T$ is a real symmetric matrix and X is an appropriate dimensions matrix, we have

$$\left(\varepsilon_j P^{-1} - Z_j^{-1} \right) Z_j \left(\varepsilon_j P^{-1} - Z_j^{-1} \right) > 0$$

i.e.,

$$-Z_j^{-1} < -2\varepsilon_j P^{-1} + \varepsilon_j^2 P^{-1} Z_j P^{-1} \ (j = 1, 2, \dots, 4).$$

This completes the proof.

REFERENCES

[1] G. Ronquillo-Lomeli, G. J. Ríos-Moreno, A. Gómez-Espinosa, L. A. Morales-Hernández, and M. Trejo-Perea, "Nonlinear identification of inverted pendulum system using Volterra polynomials," *Mech. Based Des. Struct. Mech.*, vol. 44, no. 1-2, pp. 5-15, 2016.

[2] L. B. Prasad, B. Tyagi, and H. O. Gupta, "Optimal control of nonlinear inverted pendulum system using PID controller and LQR: Performance analysis without and with disturbance input," *Int. J. Autom. Comput.*, vol. 11, no. 6, pp. 661-670, 2014.

[3] M. Fei, W. Zhao, T. C. Yang, and S. Yang, "A new experimental set-up for control study," *Trans. Inst. Meas. Control*, vol. 32, no. 3, pp. 319-330, 2010.

[4] Z. Li and Y. Zhang, "Robust adaptive motion/force control for wheeled inverted pendulums," *Automatica*, vol. 46, no. 8, pp. 1346-1353, 2010.

[5] Y. Zhao, S. Luo, L. Wang, A. Ma, and R. Fang, "Vague neural network based reinforcement learning control system for inverted pendulum," in *Int. Conf. Neural Inf. Process.*, Hong Kong, China, 2006, pp. 692-701.

[6] C. Irvene, D. Formby, S. Litchfield, and R. Beyah, "HoneyBot: A honeypot for robotic systems," *Proc. IEEE*, vol. 106, no. 1, pp. 61-70, 2018.

[7] L. Ding, Q.-L. Han, X. Ge, and X. Zhang, "An overview of recent advances in event-triggered consensus of multiagent systems," *IEEE Trans. Cybern.*, vol. 48, no. 4, pp. 1110-1123, 2018.

[8] G. Liu, "Predictive control of networked multiagent systems via cloud computing," *IEEE Trans. Cybern.*, vol. 47, no. 8, pp. 1852-1859, 2017.

[9] X. Xie, D. Yue, H. Zhang, and C. Peng, "Control synthesis of discrete-time T-S fuzzy systems: Reducing the conservatism whilst alleviating the computational burden," *IEEE Trans. Cybern.*, vol. 47, no. 9, pp. 2480-2491, 2017.

[10] X. Ge and Q.-L. Han, "Consensus of multiagent systems subject to partially accessible and overlapping Markovian network topologies," *IEEE Trans. Cybern.*, vol. 47, no. 8, pp. 1807-1819, 2017.

[11] Y.-L. Wang, Q.-L. Han, M. Fei, and C. Peng, "Network-based T-S fuzzy dynamic positioning controller design for unmanned marine vehicles," *IEEE Trans. Cybern.*, vol. 48, no. 9, pp. 2750-2763, 2018.

[12] Y. Xia, H. Yang, M. Fu, and P. Shi, "Sliding mode control for linear systems with time-varying input and state delays," *Circuits, Syst., Signal Process.*, vol. 30, no. 3, pp. 629-641, 2010.

[13] L. Zhou and Z. Yan, "H_∞ networked control of two inverted pendulums coupled by a spring," in *2015 34th China Control Conf. (CCC)*, Hangzhou, China, 2015, pp. 6794-6799.

[14] W. Wu, S. Reimann, D. Görges, and S. Liu, "Suboptimal event-triggered control for time-delayed linear systems," *IEEE Trans. Autom. Control*, vol. 60, no. 5, pp. 1386-1391, 2015.

[15] J. Hill and W. T. Park, "Real time control of a robot with a mobile camera," in *Proc. 9th Int. Symp. Ind. Robots (ISIR)*, Washington, D. C., USA, 1979, pp. 233-246.

[16] M. Vzquez-Arellano, H. W. Griepentrog, D. Reiser, and D. S. Paraforos, "3-D imaging systems for agricultural applications—A review," *Sensors*, vol. 16, no. 5, pp. 618, 2016.

[17] M. Riggio, J. Sandak, and S. Franke, "Application of imaging techniques for detection of defects, damage and decay in timber structures on-site," *Constr. Build. Mater.*, vol. 101, pp. 1241-1252, 2015.

[18] S. H. Huang and Y. C. Pan, "Automated visual inspection in the semiconductor industry: A survey," *Comput. Ind.*, vol. 66, pp. 1-10, 2015.

[19] S. Kumar, P. Singhal, and V. N. Krovi, "Computer-vision-based decision support in surgical robotics," *IEEE Des. Test*, vol. 32, no. 5, pp. 89-97, 2015.

[20] E. H. C. Harik, F. Guéin, F. Guinand, J. Brethé, H. Pelvillain, and A. Zentout, "Vision based target tracking using an unmanned aerial vehicle," in *2015 IEEE Int. Workshop Adv. Robot. Its Social Impacts (ARSO)*, Lyon, France, 2015, pp. 1-6.

[21] H. Wang, C. Vasseur, V. Koncar, A. Chamroo, and N. Christov, "Modeling and trajectory tracking control of a 2-DOF vision based inverted pendulum," *J. Control Eng. Appl. Informat.*, vol, 12, no.3, pp. 59-66, 2010.

[22] Y. W. Tu and M. T. Ho, "Design and implementation of robust visual servoing control of an inverted pendulum with an FPGA-based image co-processor," *Mechatronics*, vol. 21, no. 7, pp. 1170-1182, 2011.

[23] M. E. Magana and F. Holzapfel, "Fuzzy-logic control of an inverted pendulum with vision feedback," *IEEE Trans. Educ.*, vol. 41, no. 2, pp. 165-170, 1998.

[24] E. S. Espinoza-Quesada and L. E. Ramos-Velasco, "Visual servoing for an inverted pendulum using a digital signal processor," in *2006 IEEE*

Int. Symp. Signal Process. Inf. Technol., Vancouver, Canada, 2006, pp. 76-80.

[25] S. Kizir, H. Ocak, Z. Bingul, and C. Oysu, "Time delay compensated vision based stabilization control of an inverted pendulum," *Int. J. Innovative Comput. Inf. Control*, vol. 8, no. 12, pp. 8133-8145, 2012.

[26] A. Benitez-Morales, O. Santos, H. Romero, and L. E. Ramos-Velasco, "Suboptimal robust linear visual servoing for a delayed underactuated system," *Optim. Control Appl. Methods*, vol. 34, no. 6, pp. 696-711, 2013.

[27] X.-M. Zhang, Q.-L. Han, and X. Yu, "Survey on recent advances in networked control systems," *IEEE Trans. Ind. Informat.*, vol. 12, no. 5, pp. 1740-1752, 2016.

[28] X.-M. Zhang and Q.-L. Han, "A decentralized event-triggered dissipative control scheme for systems with multiple sensors to sample the system outputs," *IEEE Trans. Cybern.*, vol. 46, no. 12, pp. 2745-2757, 2016.

[29] D. Du, B. Qi, M. Fei, and Z. Wang, "Quantized control of distributed event-triggered networked control systems with hybrid wired-wireless networks communication constraints," *Inf. Sci.*, vol. 380, pp. 74-91, 2017.

[30] D. Du, B. Qi, M. Fei, and C. Peng, "Multiple event-triggered H_2/H_∞ filtering for hybrid networked systems with random network-induced delays," *Inf. Sci.*, vol. 325, pp. 393-408, 2015.

[31] H. Wu, L. Lou, C. C. Chen, S. Hirche, and K. Kühnlenz, "A framework of networked visual servo control system with distributed computation," in *2010 11th Int. Conf. Control Autom. Robot. Vision (ICARCV)*, Singapore, Singapore, 2010, pp. 1466-1471.

[32] C. C. Chen, H. Wu, K. Kühnlenz, and S. Hirche, "Switching control for a networked vision-based control system," *Automatisierungstechnik*, vol. 59, no. 2, pp. 124-133, 2011.

[33] H. Li, H. Wu, L. Lou, K. Kühnlenz, and O. Ravn, "Ping-pong robotics with high-speed vision system," in *2012 12th Int. Conf. Control Autom. Robot. Vision (ICARCV)*, Guangzhou, China, 2012, pp. 106-111.

[34] H. Wu, L. Lou, C. C. Chen, S. Hirche, and K. Kuhnlenz, "Cloud-based networked visual servo control," *IEEE Trans. Ind. Electron.*, vol. 60, no. 2, pp. 554-566, 2013.

[35] D. Zhang, Q.-L. Han, and X. Jia, "Network-based output tracking control for T-S fuzzy systems using an event-triggered communication scheme," *Fuzzy Sets Syst.*, vol. 273, pp. 26-48, 2015.

[36] X. Ge, Q.-L. Han, and Z. Wang, "A threshold-parameter-dependent approach to designing distributed event-triggered H_∞ consensus filters over sensor networks," *IEEE Trans. Cybern.*, vol. 49, no. 4, pp. 1148-1159, 2019.

[37] M. Zhao, C. Peng, W. He, and Y. Song, "Event-triggered communication for leader-following consensus of second-order multi-agent systems," *IEEE Trans. Cybern.*, vol. 48, vol. 6, pp. 1888-189, 2018.

[38] C. Peng, E. Tian, J. Zhang, and D. Du, "Decentralized event-triggering communication scheme for large-scale systems under network environments," *Inf. Sci.*, vol. 380, pp. 132-144, 2017.

[39] X. Ge, Q.-L. Han, and Z. Wang, "A dynamic event-triggered transmission scheme for distributed set-membership estimation over wireless sensor networks," *IEEE Trans. Cybern.*, vol. 49, no. 1, pp. 171-183, 2019.

[40] C. Peng, S. Ma, and X. Xie, "Observer-based non-PDC control for networked T-S fuzzy systems with an event-triggered communication," *IEEE Trans. Cybern.*, vol. 47, no. 8, pp. 2279-2287, 2017.

[41] C. Peng, J. Zhang, and Q.-L. Han, "Consensus of multi-agent systems with nonlinear dynamics using an integrated sampled-data-based event-triggered communication scheme," *IEEE Trans. Syst., Man, Cybern., Syst.*, vol. 49, no. 3, pp. 589-599, 2019.

[42] D. Du, X. Li, W. Li, R. Chen, M. Fei, and L. Wu, "ADMM-based distributed state estimation of smart grid under data deception and denial of service attacks," *IEEE Trans. Syst., Man, Cybern., Syst.*, to be published, doi: 10.1109/TSMC.2019.2896292.

[43] R. Chen, X. Li, H. Zhong, and M. Fei, "A novel online detection method of data injection attack against dynamic state estimation in smart grid," *Neurocomputing*, to be published, doi: 10.1016/j.neucom.2018.09.094.

[44] D. Du, R. Chen, X. Li, L. Wu, P. Zhou, and M. Fei, "Malicious data deception attacks against power systems: A new case and its detection method," *Trans. Inst. Meas. Control*, Vol. 41, no. 6, pp. 1590-1599, 2019.

[45] N. Muskinja, and B. Tovornik, "Swinging up and stabilization of a real inverted pendulum," *IEEE Trans. Ind. Electron.*, vol. 53, no. 2, pp. 631-639, 2006.

[46] P. Bakarac, M. Klauco, and M. Fikar, "Comparison of inverted pendulum stabilization with PID, LQ, and MPC control," *in 2018 Cybern. Informat.*, Lazy pod Makytou, Slovakia, 2018, pp. 1-6.

[47] S. Xu, J. Lam, and Y. Zou, "New results on delay-dependent robust H_∞ control for systems with time-varying delays," *Automatica*, vol. 42, no. 2, pp. 343-348, 2006.

[48] H. Gao, J. Wu, and P. Shi, "Robust sampled-data H_∞ control with stochastic sampling," *Automatica*, vol. 45, no. 7, pp. 1729-1736, 2009.

[49] C. Peng and Y. C. Tian, "Improved delay-dependent robust stability criteria for uncertain systems with interval time-varying delay," *IET Control Theory Appl.*, vol. 2, no. 9, pp. 752-761, 2008.

[50] Q.-L. Han, "Absolute stability of time-delay systems with sector-bounded nonlinearity," *Automatica*, vol. 41, no. 12, pp. 2171-2176, 2005.

[51] X.-M. Zhang, Q.-L. Han, A. Seuret, F. Gouaisbaut, and Y. He, "Overview of recent advances in stability of linear systems with time-varying delays," *IET Control Theory Appl.*, vol. 13, no. 1, pp. 1-16, 2019.

[52] X.-M. Zhang, Q.-L. Han, A. Seuret, and F. Gouaisbaut, "An improved reciprocally convex inequality and an augmented Lyapunov-Krasovskii functional for stability of linear systems with time-varying delay," *Automatica*, vol. 84, pp. 221-226, 2017.

[53] S. Xu, J. Lam, and X. Mao, "Delay-dependent H_∞ control and filtering for uncertain markovian jump systems with time-varying delays," *IEEE Trans. Circuits Syst. I, Reg. Papers*, vol. 54, no. 9, pp. 2070-2077, 2007.

[54] S. C. Hsu, S. F. Liang, and C. T. Lin, "A robust digital image stabilization technique based on inverse triangle method and background detection," *IEEE Trans. Consum. Electron.*, vol. 51, no. 2, pp. 335-345, 2005.

[55] L. Dias, J. Ferreira, F. Soares, G. Lopes, J. S. Esteves, M. J. Sepúlveda, and P. Garrido, "Inverted pendulum controlled by an analog PID controller: A Framework for a laboratorial experiment," in *CONTROLO 2016*, Guimarães, Portugal, 2016, pp. 857-867.

[56] R. Cao, H. Zhou, and R. Ma, "Experiment platform design cspace-based for a permanent magnet linear synchronous motor driven inverted pendulum," *Appl. Mech. Mater.*, vol. 84-85, pp. 452-456, 2011.

[57] S. Zhu, Q.-L. Han, and C. Zhang, "l_1-gain performance analysis and positive filter design for positive discrete-time Markov jump linear systems: A linear programming approach," *Automatica*, vol. 50, no. 8, pp. 2098-2107, 2014.

Supplementary Materials—Real-Time H_∞ Control of Networked Inverted Pendulum Visual Servo Systems

Dajun Du, Changda Zhang, Yuehua Song, Huiyu Zhou, Xue Li, Minrui Fei, Wangpei Li

Abstract—This is the supplementary materials of the paper "Real-Time H_∞ Control of Networked Inverted Pendulum Visual Servo Systems" submitted to IEEE Transactions on Cybernetics. Section I provides details of the designed image processing algorithm. Section II gives the statistical analysis of the computational time and errors for the statistical model. A new IPS named NIPVSS is presented in Section III.

I. IMAGE PROCESSING ALGORITHM

A. Image Capturing

In the practical experiments, to ensure the image quality with enough exposure time and an appropriate (not too long) state time-delay, the frame rate of camera is set as 100 frames per second (fps) which means that the time-consuming (exposure time) is 10 millisecond (ms) of capturing each image frame. Furthermore, to real-time continuously capture the pendulum motion images and reduce the image processing time, an event-triggered strategy is adopted, i.e., when completing the image processing of current image frame and acquiring the cart position and pendulum angle, the camera will be immediately triggered to capture the next image frame. Therefore, there are 30-50 frames images being processed per second whilst the exposure time of every image frame is 10ms.

B. Image Preprocessing

An original image captured by the camera with a uniform background is shown in Fig. A.1(a). To determine the positions of the cart and the pendulum on the image plane, the captured images are processed by a series of image processing algorithms. The visual sensor is able to provide rich information about the target and the surrounding environment, but the redundancy in the data information is severe, which takes large computational time. Firstly, the regions containing the cart and the pendulum motion areas are found from the original image, respectively, which aims at reducing data volume in order to

(a) Original image (b) Cart motion areas image (c) Pendulum motion areas image

Fig. A.1. Find the motion areas of cart and pendulum from the original image.

(a) Cart edge (b) Pendulum edge

Fig. A.2. Edge detection using The Canny edge detection algorithm.

have less image processing time. Because the camera and the inverted pendulum are fixed, the cart-inverted pendulum system is projected onto an image that has a constant size. The cart and the pendulum move within the fixed rows. Thus, it is easy to find the motion areas of the cart and pendulum based on the prior knowledge about the interval of the rows, and the results are shown in Fig. A.1(b) and (c), respectively. The standard Canny edge detection algorithm is then used to detect the edge information of the cart and the pendulum which are shown in Fig. A.2(a) and (b), respectively.

C. Cart Position Measurement

The unit of the cart position is pixel, but the unit of the experimental control parameters is physical displacement (e.g., in the state variable, the units of the cart position and pendulum angle are metre (m) and radian (rad), respectively). We need to implement the unit conversion which is based on the camera perspective projection model shown in Fig. A.3. From Fig. A.3, we see that there are four coordinate systems, i.e., the world coordinate system $O_w - X_w Y_w Z_w$, the camera coordinate system $O_c - X_c Y_c Z_c$, the pixel coordinate system $O_0 - pq$ and the image plane coordinate system $O_1 - xy$. The point O_c denotes the optical center of the camera, and the axis Z_c denotes the optical axis of the camera. Noting that the axis Z_c is perpendicular to the pixel coordinate plane and

Fig. A.3. Camera perspective projection model.

Fig. A.4. Cart position is determined using the line scan algorithm.
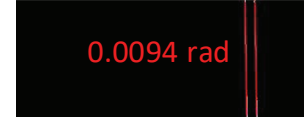
Fig. A.5. Pendulum angle is determined using the Hough Transform algorithm.

the vertical intersection is the point $O_1 (p_0, q_0)$ which is the principal point of the image in the pixel coordinate system, and the length of the line segment $O_c O_1$ denotes the focal length of the camera f, i.e., $f = O_c O_1$.

In order to obtain the physical location of the object, it is necessary to know the transformation relation between the world coordinate system and the pixel coordinate system, which is given by

$$\lambda P = K \begin{bmatrix} R & T \end{bmatrix} P_w \tag{A.1}$$

where $P = \begin{bmatrix} p & q & 1 \end{bmatrix}^T$ denotes the two-dimensional homogeneous coordinates of the image point in the pixel coordinate system, $P_w = \begin{bmatrix} X_w & Y_w & Z_w & 1 \end{bmatrix}^T$ represents the three-dimensional homogeneous coordinates of the object in the world coordinate system, and λ is a scalar factor. The unit of orthogonal matrix $R \in \Re^{3\times3}$ and vector $T \in \Re^3$ are extrinsic parameters of the camera that describe the rotation and translation between the world coordinate system and the camera coordinate system, respectively. In this study, because the camera and the inverted pendulum are relatively fixed, i.e., the world coordinate system is always coincident with the camera coordinate system, the extrinsic parameters are

$$R = \begin{bmatrix} 1 & 0 & 0 \\ 0 & 1 & 0 \\ 0 & 0 & 1 \end{bmatrix}, T = \begin{bmatrix} 0 \\ 0 \\ 0 \end{bmatrix}.$$

The matrix $K \in \Re^{3\times3}$ consists of the intrinsic parameter of the camera using camera calibration, which is given by

$$K = \begin{bmatrix} \alpha_p & s & p_0 \\ 0 & \alpha_q & q_0 \\ 0 & 0 & 1 \end{bmatrix}$$

where $\alpha_p = f/\varphi_x$, $\alpha_q = f/\varphi_y$ and φ_x, φ_y denote the physical size of each pixel in the x and y axis of the retinal coordinate system, respectively. The scalar s represents the skew factor caused by the coordinate axes of the retinal coordinate system which are not orthogonal to each other. Without loss of generality, we here assume that $s = 0$.

In this paper, since there is no rotation and translation between the world coordinate system and the camera coordinate system, the parameter λ is the Z_w coordinate of the object, which is the vertical distance defined as d (as shown in Fig. A.3) between the optical center of the camera and the vertical plane in which the swinging rod rotates freely, i.e., $\lambda = d$. The intrinsic parameters of the camera are given in Table A.I.

TABLE A.I
INTRINSIC PARAMETERS OF THE CAMERA

Parameter	Value
f	909.5pixels
d	0.9263m
α_p	1.6241×10^6pixels/m
α_q	1.6241×10^6pixels/m
s	0
p_0	334.85pixels
q_0	267.46pixels

From (A.1), we can deduce that

$$dp = \alpha_p X_w + dp_0. \tag{A.2}$$

(A.2) indicates that the horizontal coordinate X_w of the object in the world coordinate system will be obtained through a series of image processing algorithms [S1], [S2]. In order to detect the cart position in the pixel coordinate system, the line scan algorithm [S1] is used to search the vertical edge (the column coordinate) from the cart edge image shown in Fig. A.2(a). The n pixel rows q_i $(i = 1, \ldots, n)$ are arbitrarily chosen based on the prior knowledge about the interval of rows firstly, which are shown in Fig. A.4. Through these rows, their respective column coordinates p_i $(i = 1, \ldots, n)$ can be found using the line scan algorithm. Finally, the cart position is able to be determined by

$$p = \frac{1}{n} \sum_{i=1}^{n} p_i. \tag{A.3}$$

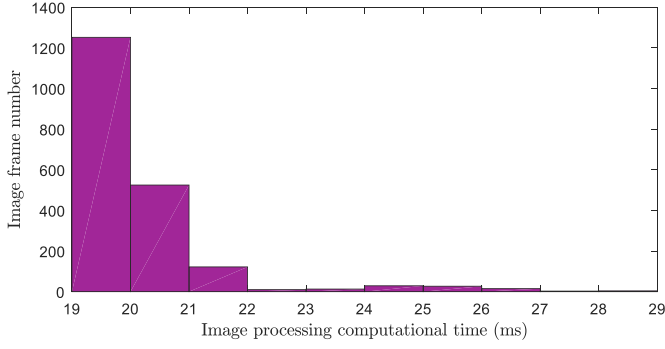Fig. A.6. Computational time's statistics.

Fig. A.7. Computational errors statistics of cart position.

The number of the rows chosen is greater than one, i.e., $n > 1$, which is aimed at reducing the detection errors. However, it will consume more time if the value of n is too large. In this paper, the value of n is set to be 3 based on the actual experimental experience.

D. Pendulum Angle Measurement

It is well known that the angle remains unchanged in the process of mapping, hence calculating the pendulum angle in the world coordinate system is equivalent to calculating the pendulum angle in the pixel coordinate system. The Hough Transform [S2], which is often used to detect straight lines from binary images, is used for the pendulum angle detection using the pendulum edge image shown in Fig. A.2(b) and the result of the detection is shown in Fig. A.5. In the actual test, the number of the detected straight lines is often greater than 2 (the 2 denotes that the binary image of the pendulum has two edges). The average incline angle of those lines is used as the pendulum angle.

II. ANALYSIS OF IMAGE PROCESSING PROBLEMS

A. Statistical Analysis of the Computational Time

It is time-consuming in the process of image acquisition, cart and pendulum positioning and state information calculation. Furthermore, the changes of the environmental background and illumination affect the image quality. In order to analyze the image processing time, 2000 images are captured firstly and then processed through a series of image processing algorithms described in the above section to estimate the cart position and pendulum angle. Meanwhile, the computational time of processing every image is recorded and the statistical result is shown in Fig. A.6. It can be seen that the variation range of the image processing time (i.e., the variation range of the state time-delay caused by image processing) is $[0.019, 0.029]\,s$. It is worth noting that different image processing algorithms or different parameters will result in variations of the state time-delay. Assuming that the $\bar{d}$ and $\underline{d}$ respectively denote the upper and lower bounds of the image processing time, then
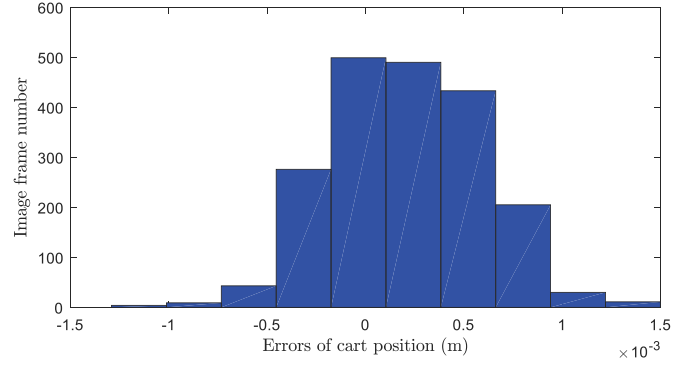
$$\underline{d} = 0.019s, \bar{d} = 0.029s. \tag{A.4}$$

B. Statistical Analysis of Computational Errors

Due to the change of the environmental background and illumination, we will have inaccurate cart positions and pendulum angles measured from the inverted pendulum motion images. In order to analyze the image processing errors, the mathematical statistical approach (i.e., a means of histogram [S3]) is used. Firstly, 2000 images are captured, and the state information is recorded using photoelectric encoders. We intend to make sure the sampling time aligned with the visual and the encoding information. In the real-time control experiments, 10 ms is used to activate the photoelectric encoders and the camera at the same time and the frame rate of the camera is set to be 100 fps. In the process of the real-time control, the motion images are captured, meanwhile, the state information measured by the photoelectric encoders is recorded, which is able to guarantee the information to be measured by the photoelectric encoders and the information of all the images is correctly corresponding. Furthermore, the cart positions and the pendulum angles are offline detected from each image using the above image processing algorithms and then compared with the benchmark to analyze the image processing errors. The statistical computational errors of the cart position, cart velocity, pendulum angle, and pendulum angular velocity are illustrated in Figs. A.7-10. They show that those computational errors are time-varied within the range of $[-0.0015, +0.0015]$, $[-0.007, +0.007]$, $[-0.075, +0.075]$ and $[-0.35, +0.35]$, respectively. We have,

$$err(t) = B_w w(t) \tag{A.5}$$

where $B_w = \begin{bmatrix} 0.0016 & 0.0071 & 0.0751 & 0.3510 \end{bmatrix}^T$, $w(t) \in (-1, +1)$ guaranteeing $w(t) \in \mathcal{L}_2(0, \infty)$.

III. BUILDING OF THE EXPERIMENTAL PLATFORM

The NIPVSS mainly includes 4 system functional modules, i.e., a pendulum (containing: one cart, one swinging rod, one slide, one belt, one AC servo motor and one servo drive), a visual sensing measurement system (containing: one industrial camera, a light source, an image parallel processing unit, a white board) and a remote visual control system.

The analysis of each system functional module is as follows:

1) Pendulum: The controlled plant of this experimental platform is a single inverted pendulum which includes one
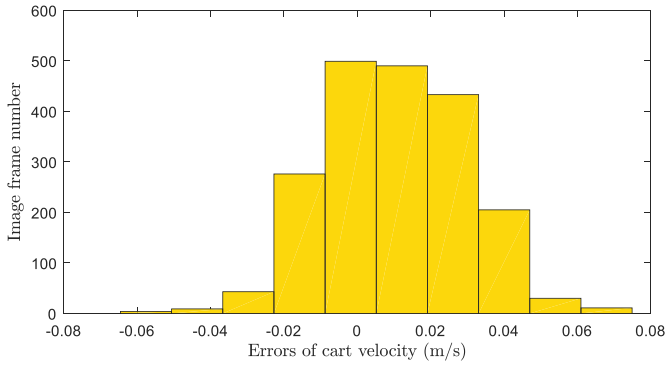
Fig. A.8. Computational errors statistics of cart velocity.
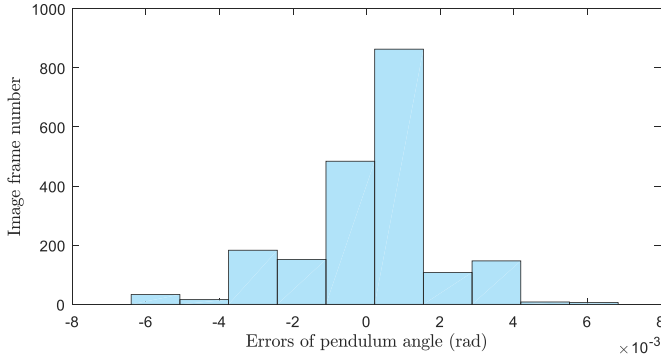

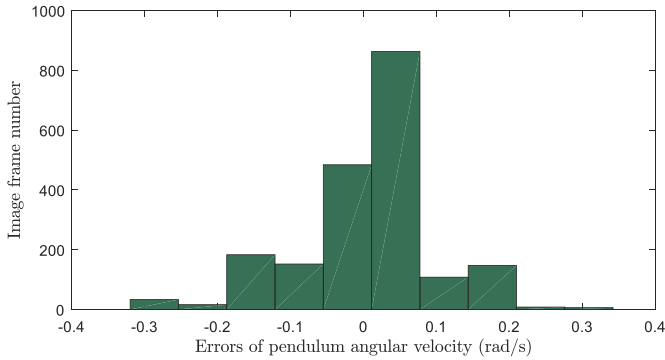Fig. A.9. Computational errors statistics of pendulum angle.

Fig. A.10. Computational errors statistics of pendulum angular velocity.

cart, one swinging rod, one slide, one belt, one AC servo motor and one servo drive. The swinging rod is hinged on the cart through the coupling and the cart moves on the rail driven by the motor through the belt.

2) Visual sensing measurement system: The visual sensing measurement system of the NIPVSS consists of one industrial camera, a light source, an image parallel processing unit and a white board. The industrial camera is set up in the opposite of the pendulum, which requires that the optical axes of the camera is perpendicular to the vertical plane in which the swinging rod rotating freely. Moreover, the vertical distance between the camera and the vertical plane can be adjusted freely. The camera is able to capture 659×492 image pixels quantized to 256 gray-levels at maximum 120 fps and the frame rate of the camera is able to be adjusted freely within

the range 120 fps according to its actual needs. The light source is a group of common LED fluorescent lamps fixated above the pendulum which ensure the height between the light source and the pendulum and the illumination intensity can be adjusted freely according to the practical requirement. The image processing unit is a personal computer and the image processing is implemented based on the software platform of Microsoft Visual Studio 2010 and OpenCV2.4.11. The white board is set up on top of the pendulum which makes sure that the swing rod fluctuates within the range of $[-10°, +10°]$.

3) Remote visual control system: The remote visual control system of the NIPVSS contains a server (including: remote visual controller) and an actuator (including: one servo drive, one AC servo motor). The client is connected to the server via a network. The state variables, i.e., the cart positions and the pendulum angles, are measured from the captured images using the image processing unit through a series of image processing algorithms and the results are shown on the control panel on the server and transmitted to the client via the network. The controlled quantity is calculated according to the control algorithm after the remote visual controller receives the state variables. Thus, the remote real-time control of single inverted pendulum system, i.e., the real-time control of NIPVSS, is implemented.

Note that the traditional photoelectric encoders are still retained in the NIPVSS even though the state variables are measured by using visual sensors in the visual servo control experiments. However, the state variables measured via photoelectric encoders can be used as a benchmark to analyze the visual servo outcomes.

REFERENCES

[S1] M. E. Magana and F. Holzapfel, "Fuzzy-logic control of an inverted pendulum with vision feedback," *IEEE Trans. Educ.*, vol. 41, no. 2, pp. 165-170, 1998.
[S2] R. O. Duda and P. E. Hart, "Use of the Hough transformation to detect lines and curves in pictures," *Commun. ACM*, vol. 15, no. 1, pp. 11-15, 1972.
[S3] M. E. Magnello, "Karl Pearson and the origins of modern statistics: An elastician becomes a statistician," *Rutherford J.*, vol. 1, 2005.